

Hot extremes have become drier in the US Southwest

Karen McKinnon (✉ kmckinnon@ucla.edu)

UCLA <https://orcid.org/0000-0003-3314-8442>

Andrew Poppick

Carleton College

Isla Simpson

NCAR <https://orcid.org/0000-0002-2915-1377>

Article

Keywords: hot extremes, US Southwest, climate change

Posted Date: November 23rd, 2020

DOI: <https://doi.org/10.21203/rs.3.rs-102766/v1>

License: © ⓘ This work is licensed under a Creative Commons Attribution 4.0 International License.

[Read Full License](#)

Version of Record: A version of this preprint was published at Nature Climate Change on June 17th, 2021.
See the published version at <https://doi.org/10.1038/s41558-021-01076-9>.

1 **Hot extremes have become drier in the US Southwest**

2 Karen A. McKinnon^{1*}, Andrew Poppick², and Isla R. Simpson³

3 ¹Department of Statistics and Institute of the Environment and Sustainability; University
4 of California, Los Angeles; Los Angeles, CA 90095; kmckinnon@ucla.edu

5 ²Department of Mathematics and Statistics; Carleton College; Northfield, MN 55057

6 ³National Center for Atmospheric Research; Boulder, CO 80305

7 **Summary paragraph**

8 The impacts of summer heat extremes are mediated by the moisture content of the at-
9 mosphere. Increases in temperatures due to human-caused climate change are generally
10 expected to increase specific humidity; however, it remains unclear how humidity extremes
11 may change, especially in climatologically dry regions. Here, using in situ measurements
12 and reanalyses, we show that specific humidity on low humidity days in the American
13 Southwest has decreased over the past seven decades, and that the greatest decreases co-
14 occur with the hottest temperatures. Hot, dry summers have anomalously low evapotran-
15 spiration that is linked to low summer soil moisture. The recent decrease in summer soil
16 moisture is explained by declines in pre-summer soil moisture, whereas the interannual vari-
17 ability is controlled by summer precipitation. Climate models project continued declines
18 in pre-summer soil moisture but increases in summer precipitation, leading to uncertainty
19 as to how summer soil moisture and hot, dry days will change in the future.

20 **Main text**

21 The semiarid climate of the Southwestern United States is caused by its location south
22 of the Pacific storm track during winter and at the eastern edge of the North Pacific
23 high during summer, which lead to climatologically low precipitation, soil moisture, and
24 humidity [1]. Against this backdrop of semiarid conditions, increased atmospheric demand
25 for moisture due to increased temperatures and/or decreased humidity can have three
26 major adverse consequences, particularly during the warm season: increases in fire risk
27 [2, 3, 4, 5, 6], increases in evaporative demand from surface reservoirs [7], and increases
28 in tree mortality [8]. While a substantial body of work has focused on the important role
29 of rising temperatures in causing each of these impacts [e.g., 9, 10, 11], there has been
30 less of a focus on changes in specific humidity, which can amplify or damp the effect of
31 temperature.

32 Here, we analyze in situ and reanalysis-based measurements of temperature and humidity
33 to determine how and why dry extremes on hot summer days have changed over the past
34 seven decades, and may change in the future. Summer is defined as July-August-September
35 (JAS), which are the climatologically warmest three months in the Southwest. Because
36 warming temperatures are an expected consequence of increasing greenhouse gases, we
37 focus on changes in the extremes of specific humidity conditional on a fixed definition of
38 a hot day. This allows for a separation of changes in the temperature-specific humidity
39 relationship – our focus in this work – from changes in specific humidity that would be
40 expected given increasing temperatures with a fixed covariance structure.

41 *Decreases in humidity are amplified at hot temperatures*

42 We first focus on estimating changes in changes in specific humidity on dry days. Our

43 approach is demonstrated at two example locations from the Integrated Surface Database
44 [ISD, 12] in Fig. 1. The middle panels show summer temperature (T') and specific humidity
45 (q') anomalies from 1973-2019 at Perry Stokes Airport, Colorado and Fresno Yosemite
46 International Airport, California. These stations were chosen because they show distinct
47 underlying T' vs. q' relationships: q' generally decreases with T' at Perry Stokes, whereas it
48 increases with T' at Fresno, although the relationships are nonlinear with different behavior
49 at the center and tails. The Southwest is a unique region because both types of relationships
50 are common, as shown in Fig. S1 with the Spearman rank correlation coefficient. We
51 quantify the dependence of q' on T' using semiparametric quantile smoothing splines [13]
52 for the 5th, 50th, and 95th percentile of q' (black lines in middle panels of Fig. 1). While
53 the focus of this work is on low humidity days, described with the 5th percentile (q'_5), we
54 present the other two percentiles for context.

55 In order to assess how the T' vs. q'_5 relationship is changing, we allow the quantile smooth-
56 ing splines to vary linearly with the lowpass filtered (1/10 year frequency cutoff) global
57 mean temperature anomaly (GMTA) using the methods of [14]. Specifically, both the
58 average value of q'_5 and the shape of the T' vs. q'_5 spline are permitted to change; the
59 complexity of the spline is selected by minimizing a high-dimensional Bayesian Informa-
60 tion Criterion [15]. The method has previously been shown to perform well for synthetic
61 data with properties similar to daily T' and q' [see Data and Methods; 14]. The fitted
62 model then provides an estimate of q'_5 for any co-occurring local T' and GMTA, so can
63 be queried to quantify how q'_5 has changed with increasing GMTA. The change in Perry
64 Stokes and Fresno is illustrated by comparing the gray and black lines in Fig. 1c,f: the
65 gray line is the T' vs. q'_5 relationship conditioned on the GMTA of 1973, whereas the black
66 line is conditioned on the GMTA of 2019. At both locations, there has been a decrease in
67 q'_5 when T' is at the 95th percentile (hereafter $q'_{5,T95}$, see the change from the gray to the

68 black line along the vertical red line in Fig. 1c,f), although they differ in other types of
69 changes. For example, Perry Stokes shows an increase in the 95th percentile of q' on hot
70 days, whereas Fresno shows a decrease.

71 We perform the same analysis at all high-quality ISD stations in the United States with
72 near-continuous records from 1973-2019 (see Data and Methods), with a focus on changes
73 in $q'_{5,T95}$. Across the Southwest, $q'_{5,T95}$ has decreased by an average of 1.04 g/kg per degree
74 increase GMTA, or 0.94 g/kg since 1973 (Fig. 2a). The distribution of trends is skewed
75 towards greater decreases, such that a quarter of the stations in the Southwest, primarily in
76 California, have decreases in excess of 2 g/kg per degree increase GMTA. To contextualize
77 these changes, the empirical 5th percentile of specific humidity on hot days averaged across
78 ISD stations in the Southwest for 1973-2019 is 4.31 g/kg; thus, the average magnitude of
79 the decreases in specific humidity on hot, dry days is over 20% of the baseline value.

80 It is also possible to examine how q'_5 has changed conditional on different percentiles of
81 T' . A consistent picture emerges across the region where the magnitude of the decrease
82 in q'_5 increases with the co-occurring T' (Fig. 2b). On average, q'_5 has increased when
83 T' is low (< 26 th percentile), exhibits a small decrease of 0.27 g/kg per degree increase
84 GMTA on days with the median T' , and shows increasingly large decreases at higher T' ,
85 with an average decrease of 1.32 g/kg per degree increase GMTA when T' is at the 99th
86 percentile. Due to this amplification, analyses of changes in q'_5 without accounting for the
87 relationship with T' would underestimate the changes on hot days, when the impacts are
88 greatest.

89 *Hot days have gotten drier since 1950*

90 The foregoing analysis offers the advantage of using direct measurements from weather sta-
91 tions of the near-surface layer, but is hindered by data availability. Spatially, only 28 high-

92 quality stations are available across the region, which is topographically diverse; further,
93 all stations are at airports, raising concerns that they are not representative of the region
94 as a whole. Temporally, the relatively short duration of the data record (48 years, 1973-
95 2019) provides only a limited view into the potential role of low-frequency ocean-driven
96 variability versus anthropogenic forcings in contributing to the observed trends.

97 To address both of these issues, we first turn to additional sources of information. To
98 allow for intercomparison between data sources in terms of both trends and variability,
99 we define an annual amplification index for the full Southwest region. The index is the
100 average probability across the region of having a dry day given the occurrence of a hot day.
101 A hot day is defined at each location as a day in the 85th-95th percentile range (combined
102 red and orange polygons in Fig. 1b,e) and a dry day has a specific humidity below the
103 temperature-dependent 10th quantile of specific humidity for a GMTA of zero (orange
104 polygon in Fig. 1b,e). The thresholds for hot and dry are less extreme than the percentiles
105 used in the prior analysis because calculating the probability of extreme events through
106 empirical counts is noisier than employing a semiparametric model. Counts are summed
107 across stations, weighted by the area they represent, to produce the annual amplification
108 index.

109 As expected, the amplification index calculated using the ISD data from 1973-2019, ISD_{1973} ,
110 shows an increase in the probability of having low humidity conditions on hot days, par-
111 ticularly post-2000 (Fig. 3a). In addition, there is substantial interannual variability, with
112 1979, 1987-1989, and 1993-1995 all exhibiting above-average dryness early in the record.
113 We next calculate the same index using the ERA5 reanalysis [16] in order to assess if the
114 index is biased by the spatial distribution and limited number of stations. The two indices
115 closely track each other in both their variability and their trend, and are correlated at 0.88
116 across their shared period of record of 1979-2019, suggesting that the signal of drying is

117 sufficiently large-scale across the Southwest that it can be captured by a small number of
118 station measurements. Finally, we extend the time series record using the 12 stations in the
119 region that have measurements beginning in 1950 (ISD₁₉₅₀, Fig. S2, Data and Methods)
120 and the JRA-55 reanalysis [17], the only third-generation reanalysis product that begins
121 before 1979 as of this writing. All four estimates of the index paint a similar picture: the
122 ISD₁₉₅₀ index is correlated with the ISD₁₉₇₃ and ERA5 indices at 0.82 and 0.75, and the
123 JRA-55 index is correlated with the ISD₁₉₅₀, ISD₁₉₇₃, and ERA5 indices at 0.72, 0.90, and
124 0.92, respectively.

125 Using all four data sources (ERA5, JRA-55, ISD₁₉₅₀, and ISD₁₉₇₃), we calculate a single
126 average amplification index (black line in both panels of Fig. 3) that spans seven decades.
127 Because the number of datasets being averaged increases over time, we expect more vari-
128 ability during the earlier period; however, the subsequent results are qualitatively similar
129 when using the ISD₁₉₅₀ index alone. By extending the time series before the 1970s, we can
130 see that multiple years in the 1950-1965 period exhibited an increased probability of dry
131 extremes on hot days. This phasing and behavior is consistent with Atlantic Multidecadal
132 Variability (AMV): the positive phase of the AMV, which occurred from roughly 1926-
133 1965 and 1998-2014, causes increased subsidence, decreased precipitation, and decreased
134 humidity in the Southwest [18, 19, 20]. However, the recent uptick is unprecedented in
135 the record, suggesting an additional role of human influence. As an initial estimate of
136 the relative roles of these two factors, we fit a multiple linear regression model for the
137 amplification index using the AMV index and GMTA, both of which are lowpass filtered
138 with a frequency cutoff of 1/10 years. The regression coefficient associated with predicting
139 the amplification index with the AMV is twice that for GMTA (Table S1), but the range
140 of GMTA over the 1950-2019 period is 0.96°C, compared to 0.44°C for the AMV, so the
141 total change explained by each factor in the regression model is very similar. A regres-

142 sion model that also includes the December-January-February Niño 3.4 index and/or the
143 annual Pacific Decadal Oscillation index does not show a significant contribution of either
144 mode.

145 *Summers with hot, dry extremes have low soil moisture*

146 We next turn to explaining the physical mechanisms that lead to increases in the probability
147 of dry conditions on hot days. Decreases in near-surface atmospheric humidity can come
148 from three sources: (1) increases in horizontal and/or vertical moisture divergence; (2)
149 decreases in evapotranspiration; and/or (3) increases in precipitation. Due to our focus
150 on the driest days in an already semiarid region, precipitation is not a relevant factor
151 for directly causing humidity levels well below saturation, leaving us to assess (1) and
152 (2).

153 We first consider the potential role of horizontal moisture divergence. Using ERA5, we cal-
154 culate the spatial pattern of vertically integrated moisture divergence anomalies (VIMD')
155 associated with low humidity years as the difference between a composite of the summer
156 VIMD' during the years in the top tercile (33%) of the ERA5-based amplification index,
157 minus those in the bottom tercile. In addition, we compare the time series of the ampli-
158 fication index to that of the summer-averaged, domain-averaged VIMD' (Fig. S3). The
159 composite map does not show a coherent pattern of divergence or convergence across the
160 Southwest, and neither the raw nor detrended time series are significantly correlated with
161 the raw or detrended amplification index. Since moisture divergence in the Southwest is
162 closely related to the North American monsoon, which varies in its strength throughout the
163 summer season, we additionally compare month-by-month VIMD' to the amplification in-
164 dex. The July composite map shows a coherent region of increased divergence in Arizona,
165 New Mexico, and Colorado, and the detrended July VIMD' is weakly but significantly

166 (Pearson's r : 0.47, p -value: 0.001) correlated with the detrended amplification index (not
167 shown). This suggests a role of the North American monsoon for the interannual variability
168 in the amplification index that we will return to below.

169 We next examine whether near-surface drying is associated with a vertical redistribution of
170 moisture from the near-surface to other parts of the atmospheric column through creating
171 top tercile of the ERA5 amplification index minus bottom tercile composites of the average
172 vertical profile of specific humidity between 850 and 200 hPa over the Southwest (note that
173 47% of the Southwest domain is below 850 hPa on average; for all levels, gridboxes where
174 a given level is below the surface are masked). The vertical profile shows negative specific
175 humidity anomalies throughout the column (Fig. S3), indicating that vertical redistribution
176 of moisture cannot explain the near-surface behavior.

177 Having found only weak relationships between moisture divergence and the amplification
178 index, we turn to our second physical mechanism, decreases in evapotranspiration. The
179 composite map and time series, made in the same manner as for $VIMD'$, show that years
180 with a high number of dry extremes on hot days are associated with lower than average
181 evapotranspiration (the sign of evapotranspiration is defined here as positive from surface
182 to atmosphere) across the Southwest (Fig. 4a). The time series of Southwest-average evap-
183 otranspiration and the amplification index are significantly correlated both in their raw
184 and detrended versions (Fig. 4b), suggesting the importance of moisture from the land
185 surface in controlling the probability of dry conditions. The variability and recent decrease
186 in evapotranspiration is reflective of surface soil moisture (Fig. 4c,d): due to the aridity of
187 the Southwest, summer evapotranspiration is moisture-limited [21, 22, 23], so evapotran-
188 spiration is responding to, rather than driving, surface soil moisture variability.

189 Since evapotranspiration is limited by surface soil moisture, what drives the variability and

190 trend in the soil moisture itself? Summer soil moisture is controlled by a simple balance
191 between (1) the initial soil moisture at the beginning of the summer season, and (2) changes
192 in moisture availability during summer. Because evapotranspiration in the Southwest is
193 moisture-limited and the contribution of runoff is an order of magnitude smaller than the
194 other variables (Fig. S4), factor (2) is dominated by changes in precipitation. Using soil
195 moisture from ERA5 and precipitation from the Global Precipitation Climatology Centre
196 [GPCC, 24], we indeed find that summer soil moisture is very well predicted (Pearson’s
197 r : 0.93) by June top 1m soil moisture and JAS precipitation (Fig. 4i). June soil moisture
198 has been decreasing since 1979, consistent with the trend in summer surface soil moisture
199 (Fig. 4e,f). On the other hand, summer precipitation does not exhibit a significant trend
200 during the ERA5 period, but better explains the interannual variability around the trend
201 through its ability to recharge soil moisture levels throughout the summer (Fig. 4g,h).

202 To link these controls on summer soil moisture back to hot, dry days, we fit a multiple
203 linear regression model for the amplification index using June soil moisture and summer
204 precipitation as predictors. Using soil moisture from either ERA5 (1979-2019), JRA-55
205 (1958-2019), or NASA Global Land Data Assimilation System Version 2.0 [GLDAS2.0,
206 1950-2014 25], and precipitation from GPCC, the model captures the low-frequency vari-
207 ability and recent uptick in the amplification index, although it tends to overestimate the
208 index in the 1970s and underestimate it in the recent period (compare the colored and
209 black lines in Fig. 3b). The regression coefficients for both soil moisture and precipitation
210 are significant in all cases (see Table S1), except for GLDAS2.0 soil moisture, which has a
211 weaker relationship with the amplification index (p-value: 0.014) because it shows a smaller
212 recent decrease in soil moisture than the other two datasets (Fig. 5a). The predicted ampli-
213 fication index using ERA5, JRA-55, and GLDAS2.0 is correlated with the observed average
214 amplification index at 0.63, 0.52, and 0.51 for their respective periods.

215 *Future projections are uncertain due to precipitation*

216 We finally consider the implications of our results for future projections. In our analysis,
217 we have found that June soil moisture has been decreasing since the 1980s (Fig. 5a), which
218 has led to decreased summer soil moisture, decreased evapotranspiration, and an increase
219 in the probability of dry conditions on hot days (recall Fig. 4). While precipitation plays an
220 important role in the interannual variability of moisture availability, it does not yet appear
221 to have a significant (Fig. 4h) or forced [e.g., 26] trend. How will these factors change in
222 the future? To provide one answer to this question, we use the CMIP6 archive [27] to
223 estimate forced changes from 1950 to 2100 as the mean of the available simulations for the
224 historical and SSP5-8.5 future scenarios [28]. Consistent with ERA5, summer surface soil
225 moisture in the CMIP6 models is well-predicted by June column soil moisture and summer
226 precipitation, with an ensemble median correlation of 0.95 between the fitted and actual
227 summer soil moisture. The CMIP6 ensemble mean shows a decrease in June soil moisture
228 beginning around 1980, and the majority (79%) of models project a negative trend over
229 2015-2100 (Fig. 5), reflecting decreased snowpack and increased evapotranspiration during
230 winter and spring [29, 30]. In addition, 68% of models project an increase in summer
231 precipitation, which stands in contrast to a current lack of forced precipitation trend. As
232 a result, the models are split about whether summer soil moisture will increase or decrease
233 (Fig. 5b). Further, changes in plant physiology driven by increased CO₂ levels has the
234 potential to alter the historical link between soil moisture and evapotranspiration if plants
235 close their stomata and increase their water use efficiency [31]. Thus, while the trend in
236 summer soil moisture and the probability of dry conditions on hot days appears driven
237 by pre-summer soil moisture in the historical record, future conditions will additionally
238 depend on summer precipitation and the response of the biosphere to elevated CO₂.

239 In summary, although specific humidity is expected to increase overall with warming due

240 to greater evaporation from the ocean and the increased water vapor holding capacity of
241 the atmosphere, we find that it has decreased during the summer over the semiarid South-
242 west since 1950, with the greatest decreases co-occurring with hot days. In the historical
243 record, the probability of dry conditions on hot days, quantified by the amplification in-
244 dex, exhibits low-frequency variability consistent with the AMV, and a recent uptick that
245 is unprecedented since 1950, although a formal attribution study is needed to parse the
246 role of these factors versus others, such as internal atmospheric variability, in contributing
247 to the observed changes. The proximal cause of the recent increase in the amplification
248 index is a decrease in moisture fluxes from the surface due to low summer soil moisture,
249 which follows from decreases in June soil moisture. Forecasting the future of Southwest
250 dry extremes, however, requires reducing climate model spread in soil moisture and rainfall
251 projections.

252 **Methods**

253 **Integrated Surface Database data** Temperature and humidity data are from the In-
254 tegrated Surface Database [ISD, 12] provided by the National Centers for Environmental
255 Information. The database is composed of in situ weather station measurements taken on
256 sub-daily timescales, and is the only direct source of publicly available non-remotely sensed
257 humidity data for the United States. Humidity information is provided via measurements
258 of dew point. We mark any measurement with a suspect quality control flag as missing. In
259 particular, we remove data points with a source flag of 2, A, B, O, or 9; a report type flag of
260 99999; a call sign flag of 99999; and a quality control flag of V01. We additionally remove
261 days that do not have four or more valid observations. Our ISD-based analysis focused
262 on two time periods: 1973-2019 and 1950-2019. There is a large increase in the number
263 of weather stations reporting to the ISD database beginning in 1973, so the shorter time
264 period allows for greater selectivity and more complete spatial coverage. In both cases, a
265 given weather station is only included in the analysis if at least 80% of years have less than
266 20% missing data in both temperature and dew point for the summer season of each year,
267 and have some measurements during the first and last three years of the time period of
268 interest. For the 1973-2019 period, we additionally remove stations that have more than
269 one missing year in a row.

270 **Calculating daily-average specific humidity** Daily average specific humidity (q in
271 g/kg) is calculated from sub-daily (at least six hourly) values of dew point (T_d in degrees
272 Celsius) and pressure (p in hPa) using the following approximation [32]:

$$e = 6.112 \exp\left(\frac{17.67T_d}{T_d + 243.5}\right) \quad (1)$$

$$q = 1000 \frac{0.622e}{p - 0.378e}. \quad (2)$$

273 **Anomaly calculation** Daily temperature and specific humidity are considered as anoma-
 274 lies from the climatological seasonal cycle, with the seasonal cycle calculated as the first
 275 three seasonal harmonics of the daily climatology for temperature, and ten harmonics for
 276 specific humidity. The larger number of bases for specific humidity is necessary in this re-
 277 gion because the onset of the Southwestern monsoon can lead to a rapid increase in specific
 278 humidity over a short period of time.

279 **ERA5 data** For the calculation of the amplification index using ERA5 [16], we use 6-
 280 hourly 2-meter air temperature, 2-meter dew point, and surface pressure; surface pressure
 281 and dew point are used to calculate specific humidity as with the ISD data. To un-
 282 derstand the causes of the variability and trend in the amplification index, we use the
 283 monthly-averaged reanalysis for evapotranspiration, vertically integrated moisture diver-
 284 gence, runoff, and soil moisture. The effective accumulation period for evapotranspiration,
 285 vertically integrated moisture divergence and runoff is one day. We group soil moisture into
 286 surface (swvl1, 0-7cm) and top 1m (swvl1, swvl2, and swvl3). All ERA5-based analyses
 287 span 1979-2019.

288 **JRA-55 data** For the calculation of the amplification index in JRA-55 [17], we use 6-
 289 hourly 2-meter air temperature and 2-meter specific humidity. We calculate the index
 290 using both the analysis and forecast variables, the former which incorporates screen-level
 291 observations through optimal interpolation, but is not subsequently coupled back into the
 292 forecast. The results using the analysis output are presented in the main paper. The
 293 amplification index calculated using the forecast variables alone, however, is inconsistent
 294 with all other estimates of the amplification index in both the low-frequency and high-
 295 frequency variability. JRA-55 soil moisture is provided as a wetness fraction for three

296 layers of soil. We integrate the soil wetness fraction across the top 1m of soil assuming a
297 vegetation type of broadleaf shrubs with groundcover, which is dominant in the Southwest
298 [e.g. Fig. 5 in 33]. The layer thicknesses for broadleaf shrubs with groundcover are 0.02m,
299 0.47m, and 1m. All JRA-55-based analyses span 1958-2019.

300 **GLDAS data** The GLDAS-based regression model in Fig. 3b uses the top 1m soil moisture
301 for the 1950-2014 period, where the end date is limited by the availability of GLDAS 2.0.
302 GLDAS 2.0 is forced by the Princeton meteorological forcing dataset [34], and does not
303 use data assimilation.

304 **CMIP6 data** We use the following models from the CMIP6 archive, based on their hav-
305 ing at least one ensemble member with monthly-average total column soil moisture (mrso),
306 surface soil moisture (mrsos), and precipitation (pr) for both the historical and SSP5-8.5
307 scenarios: ACCESS-CM2, ACCESS-ESM1-5, BCC-CSM2-MR, CAMS-CSM1-0, CESM2,
308 CESM2-WACCM, CMCC-CM2-SR5, CNRM-CM6-1, CNRM-CM6-1-HR, CNRM-ESM2-
309 1, CanESM5, CanESM5-CanOE, EC-Earth3, EC-Earth3-Veg, FGOALS-f3-L, FGOALS-
310 g3, GFDL-CM4, GFDL-ESM4, GISS-E2-1-G, IPSL-CM6A-LR, MIROC-ES2L, MIROC6,
311 MPI-ESM1-2-HR, MPI-ESM1-2-LR, MRI-ESM2-0, NorESM2-LM, NorESM2-MM, and
312 UKESM1-0-LL. For CMIP6 models that have more than one ensemble member, we first
313 average the available ensemble members before calculating the ensemble mean such that
314 each model contributes equally to our analysis. The standardized soil moisture anomalies
315 in Fig. 5a are calculated using the 1979-2014 period as a reference, to match the overlapping
316 availability of the three observation-based datasets. The trends in Fig. 5b are calculated
317 over the SSP5-8.5 scenario only, 2015-2100.

318 **Global mean temperature and sea surface temperature modes** Global mean tem-
319 perature anomalies (GMTA) are from the Berkeley Earth Surface Temperature dataset

320 [35]. The Atlantic Multidecadal Variability (AMV) index is calculated as per [36] by re-
 321 moving the near-global mean (60°S-60°N) sea surface temperature (SST) anomaly from the
 322 SST anomaly over the North Atlantic (0°-60°N, 80°W-0°) at each timestep using monthly
 323 average data from ERSSTv5 [37]. All analyses with GMTA and AMV use a lowpass filtered
 324 time series calculated with a third-order Butterworth filter with a cutoff frequency of 1/10
 325 years. The Niño 3.4 and Pacific Decadal Oscillation indices are provided by the National
 326 Center for Environmental Information.

327 **Amplification index** The amplification index is the empirical count of hot, dry days
 328 normalized by hot days in a given summer. Because some gridboxes and stations may not
 329 have any hot days in a given summer, we first sum the counts across stations or gridboxes,
 330 weighted by the area they represent, before performing the division.

331 **Quantile smoothing splines method** To assess changes in the distribution of specific
 332 humidity anomalies conditional on the co-occurring local temperature anomalies and global
 333 mean temperature anomalies (GMTA), we use quantile smoothing splines [13] that can
 334 vary linearly with GMTA. Specifically, we model a given quantile, τ , of specific humidity
 335 anomalies on day t as

$$q'_\tau(t) = \beta_{0,\tau} + s_{0,\tau}(T'(t)) + \beta_{1,\tau}G'(t) + G'(t)s_{1,\tau}(T'(t)) \quad (3)$$

336 where $T'(t)$ is the co-occurring temperature and $G'(t)$ is the lowpass filtered GMTA. The first
 337 two terms on the right-hand side summarize the quantiles of specific humidity anomalies,
 338 including the dependence on local temperature anomalies, for a GMTA of zero. The second
 339 two terms allow the quantiles of specific humidity anomalies, including the dependence
 340 on local temperature anomalies, to change linearly with GMTA. The terms $s_{0,\tau}(T'(t))$
 341 and $s_{1,\tau}(T'(t))$ are quantile smoothing splines that summarize the potentially nonlinear

342 relationship between a given quantile of specific humidity and temperature anomalies. The
343 complexity of the spline is controlled by a regularization parameter, which was selected
344 in [14] through minimization of a high-dimensional Bayesian Information Criterion [15].
345 Here, we draw upon the results of [14] and model the log of the regularization parameter
346 as linearly related to the standard deviation of the temperature anomalies at each station
347 (see their Fig. S5). We fit the 5th, 10th, 50th, 90th, and 95th percentile of specific humidity
348 anomalies, although the focus of the work is primarily on the 5th percentile. A non-crossing
349 constraint is enforced during the fitting procedure following [38] such that a lower percentile
350 of specific humidity anomalies cannot be higher than a higher one at any time. Fitting
351 the changes in $q'_r(t)$ as linearly related to GMTA rather than time reduces the influence of
352 internal variability in the trend estimates and allows for the analysis of longer time periods
353 over which anthropogenic influence may not have been linear.

354 **Spatial domain and area weighting** We focus on the American Southwest, defined
355 as including Colorado, New Mexico, Utah, Arizona, Nevada, and non-coastal California
356 (see outline in Fig. 2). Values presented as averages over the domain are weighted by
357 approximations of the amount of area represented by each weather station or gridbox. For
358 the 1973-2019 period, during which stations are more plentiful, the station weights are the
359 areas associated with each station after performing a Voronoi tessellation on all stations in
360 the United States. For the 1950-2019 period, due to the reduced number of stations that
361 border the Western US domain, the station weights are instead calculated as the minimum
362 distance between a station and any other station within the Southwest domain. Results
363 are insensitive to reasonable choices of station weighting. For the reanalyses, gridboxes are
364 weighted by the cosine of latitude.

365 **Correlations and significance** All correlation values are Pearson correlation coefficients,
366 with the exception of Fig. S1, which uses the Spearman rank correlation due to the nonlin-

367 earity in the temperature-specific humidity relationship. The effective degrees of freedom
368 used for the estimation of p-values is calculated as $n_{\text{eff}} = \frac{1-\phi^2}{1+\phi^2}N - 2$ for the raw corre-
369 lations, and $n_{\text{eff}} = \frac{1-\phi^2}{1+\phi^2}N - 3$ for the detrended correlations [39], where the reduction of
370 two degrees of freedom is due to controlling for the mean and variance, and the reduction
371 of an additional degree of freedom in the detrended case is due to controlling for a linear
372 time trend. The value of ϕ is the empirical lag-1 autocorrelation coefficient of the residuals
373 for the regression model associated with each correlation value ($y = \beta_0 + \beta_1x + \epsilon$ for raw
374 correlations, and $y = \beta_0 + \beta_1x + \beta_2t + \epsilon$ for detrended correlations). All p-values are one-
375 sided, because the expected direction of the relationships is *a priori* known. Unless stated
376 otherwise, significance is assessed at the 0.01 level.

377 **Acknowledgements** K.A.M acknowledges support from the National Science Foundation
378 (award number 1939988). JRA-55 data were provided by the Research Data Archive
379 of the Computational and Information Systems Laboratory at the National Center for
380 Atmospheric Research. Analysis was performed on the Casper cluster supported by by
381 NCAR's Computational and Information Systems Laboratory. NCAR is supported by
382 grants from the National Science Foundation.

383 **Author Contributions** K.A.M. conceived the study, performed the analysis, and wrote
384 the manuscript. A.P. contributed to the development of the method and provided commen-
385 tary on the manuscript. I.R.S. provided feedback on the analysis and manuscript.

386 **Competing Interests statement** The authors declare no competing interests.

387 **Data and code availability** Code to fit the noncrossing quantile smoothing splines model
388 is available at https://github.com/karenamckinnon/humidity_variability. Code to
389 reproduce the figures in the paper will be made publicly available on github upon pub-
390 lication. The Integrated Surface Database, ERA5, and JRA-55 datasets are all publicly
391 available.

392 References

- 393 [1] Seager, R. *et al.* Whither the 100th Meridian? The Once and Future Physical and
394 Human Geography of America’s Arid–Humid Divide. Part I: The Story So Far. *Earth*
395 *Interactions* **22**, 1–22 (2018).
- 396 [2] Bradshaw, L. S., Deeming, J. E., Burgan, R. E. & Cohen, J. D. National Fire-Danger
397 Rating System–Technical Documentation. *USDA Forest Service General Technical*
398 *Report INT* **169**, 44 (1983).
- 399 [3] Evett, R. R., Mohrle, C. R., Hall, B. L., Brown, T. J. & Stephens, S. L. The effect
400 of monsoonal atmospheric moisture on lightning fire ignitions in southwestern North
401 America. *Agricultural and Forest Meteorology* **148**, 1478–1487 (2008).
- 402 [4] Fosberg, M. A. Weather in wildland fire management: the fire weather index. *US*
403 *Forest Service Reprints* (1978).
- 404 [5] Flannigan, M. & Harrington, J. A study of the relation of meteorological variables to
405 monthly provincial area burned by wildfire in Canada (1953–80). *Journal of Applied*
406 *Meteorology* **27**, 441–452 (1988).
- 407 [6] Williams, A. P. *et al.* Causes and implications of extreme atmospheric moisture de-
408 mand during the record-breaking 2011 wildfire season in the southwestern United
409 States. *Journal of Applied Meteorology and Climatology* **53**, 2671–2684 (2014).
- 410 [7] Friedrich, K. *et al.* Reservoir evaporation in the Western United States: current
411 science, challenges, and future needs. *Bulletin of the American Meteorological Society*
412 **99**, 167–187 (2018).
- 413 [8] Eamus, D., Boulain, N., Cleverly, J. & Breshears, D. D. Global change-type drought-

- 414 induced tree mortality: vapor pressure deficit is more important than temperature per
415 se in causing decline in tree health. *Ecology and Evolution* **3**, 2711–2729 (2013).
- 416 [9] Allen, C. D. *et al.* A global overview of drought and heat-induced tree mortality
417 reveals emerging climate change risks for forests. *Forest Ecology and Management*
418 **259**, 660–684 (2010).
- 419 [10] Williams, A. P. *et al.* Temperature as a potent driver of regional forest drought stress
420 and tree mortality. *Nature Climate Change* **3**, 292–297 (2013).
- 421 [11] Abatzoglou, J. T. & Williams, A. P. Impact of anthropogenic climate change on
422 wildfire across western US forests. *Proceedings of the National Academy of Sciences*
423 **113**, 11770–11775 (2016).
- 424 [12] Smith, A., Lott, N. & Vose, R. The integrated surface database: Recent developments
425 and partnerships. *Bulletin of the American Meteorological Society* **92**, 704–708 (2011).
- 426 [13] Koenker, R., Ng, P. & Portnoy, S. Quantile smoothing splines. *Biometrika* **81**, 673–680
427 (1994).
- 428 [14] McKinnon, K. A. & Poppick, A. Estimating changes in the observed relationship be-
429 tween humidity and temperature using noncrossing quantile smoothing splines. *Jour-
430 nal of Agricultural, Biological and Environmental Statistics* 1–23 (2020).
- 431 [15] Lee, E. R., Noh, H. & Park, B. U. Model selection via Bayesian information criterion
432 for quantile regression models. *Journal of the American Statistical Association* **109**,
433 216–229 (2014).
- 434 [16] Hersbach, H. *et al.* The ERA5 global reanalysis. *Quarterly Journal of the Royal*
435 *Meteorological Society* **146**, 1999–2049 (2020).

- 436 [17] Kobayashi, S. *et al.* The JRA-55 reanalysis: General specifications and basic charac-
437 teristics. *Journal of the Meteorological Society of Japan. Ser. II* **93**, 5–48 (2015).
- 438 [18] Sutton, R. T. & Hodson, D. L. Atlantic Ocean forcing of North American and Euro-
439 pean summer climate. *Science* **309**, 115–118 (2005).
- 440 [19] Kushnir, Y., Seager, R., Ting, M., Naik, N. & Nakamura, J. Mechanisms of tropical
441 Atlantic SST influence on North American precipitation variability. *Journal of Climate*
442 **23**, 5610–5628 (2010).
- 443 [20] Ruprich-Robert, Y. *et al.* Impacts of the Atlantic multidecadal variability on North
444 American summer climate and heat waves. *Journal of Climate* **31**, 3679–3700 (2018).
- 445 [21] Teuling, A. *et al.* A regional perspective on trends in continental evaporation. *Geo-*
446 *physical Research Letters* **36** (2009).
- 447 [22] Seneviratne, S. I. *et al.* Investigating soil moisture–climate interactions in a changing
448 climate: A review. *Earth-Science Reviews* **99**, 125–161 (2010).
- 449 [23] Vargas Zeppetello, L. R., Battisti, D. S. & Baker, M. B. The Origin of Soil Moisture
450 Evaporation “Regimes”. *Journal of Climate* **32**, 6939–6960 (2019).
- 451 [24] Schneider, U., Fuchs, T., Meyer-Christoffer, A. & Rudolf, B. Global precipitation
452 analysis products of the GPCC. *Global Precipitation Climatology Centre (GPCC),*
453 *DWD, Internet Publikation* **112** (2008).
- 454 [25] Rodell, M. *et al.* The global land data assimilation system. *Bulletin of the American*
455 *Meteorological Society* **85**, 381–394 (2004).
- 456 [26] Lehner, F., Deser, C., Simpson, I. R. & Terray, L. Attributing the US Southwest’s
457 recent shift into drier conditions. *Geophysical Research Letters* **45**, 6251–6261 (2018).

- 458 [27] Eyring, V. *et al.* Overview of the Coupled Model Intercomparison Project Phase 6
459 (CMIP6) experimental design and organization. *Geoscientific Model Development* **9**,
460 1937–1958 (2016).
- 461 [28] O’Neill, B. C. *et al.* The scenario model intercomparison project (ScenarioMIP) for
462 CMIP6. *Geoscientific Model Development* **9**, 3461–3482 (2016).
- 463 [29] Mankin, J. S., Smerdon, J. E., Cook, B. I., Williams, A. P. & Seager, R. The Curious
464 Case of Projected Twenty-First-Century Drying but Greening in the American West.
465 *Journal of Climate* **30**, 8689–8710 (2017).
- 466 [30] Cook, B. *et al.* Twenty-first century drought projections in the CMIP6 forcing sce-
467 narios. *Earth’s Future* **8** (2020).
- 468 [31] Swann, A. L. Plants and drought in a changing climate. *Current Climate Change*
469 *Reports* **4**, 192–201 (2018).
- 470 [32] Bolton, D. The computation of equivalent potential temperature. *Monthly Weather*
471 *Review* **108**, 1046–1053 (1980).
- 472 [33] Zheng, W. *et al.* Improvement of daytime land surface skin temperature over arid
473 regions in the NCEP GFS model and its impact on satellite data assimilation. *Journal*
474 *of Geophysical Research: Atmospheres* **117** (2012).
- 475 [34] Sheffield, J., Goteti, G. & Wood, E. F. Development of a 50-year high-resolution global
476 dataset of meteorological forcings for land surface modeling. *Journal of Climate* **19**,
477 3088–3111 (2006).
- 478 [35] Rohde, R. *et al.* Berkeley Earth Temperature Averaging Process. *Geoinformatics*
479 *Geostatistics An Overview* **1**, 20–100 (2013).

- 480 [36] Trenberth, K. E. & Shea, D. J. Atlantic hurricanes and natural variability in 2005.
481 *Geophysical Research Letters* **33** (2006).
- 482 [37] Huang, B. *et al.* Extended reconstructed sea surface temperature, version 5
483 (ERSSTv5): upgrades, validations, and intercomparisons. *Journal of Climate* **30**,
484 8179–8205 (2017).
- 485 [38] Liu, Y. & Wu, Y. Stepwise multiple quantile regression estimation using non-crossing
486 constraints. *Statistics and its Interface* **2**, 299–310 (2009).
- 487 [39] Bretherton, C. S., Widmann, M., Dymnikov, V. P., Wallace, J. M. & Bladé, I. The
488 effective number of spatial degrees of freedom of a time-varying field. *Journal of*
489 *Climate* **12**, 1990–2009 (1999).

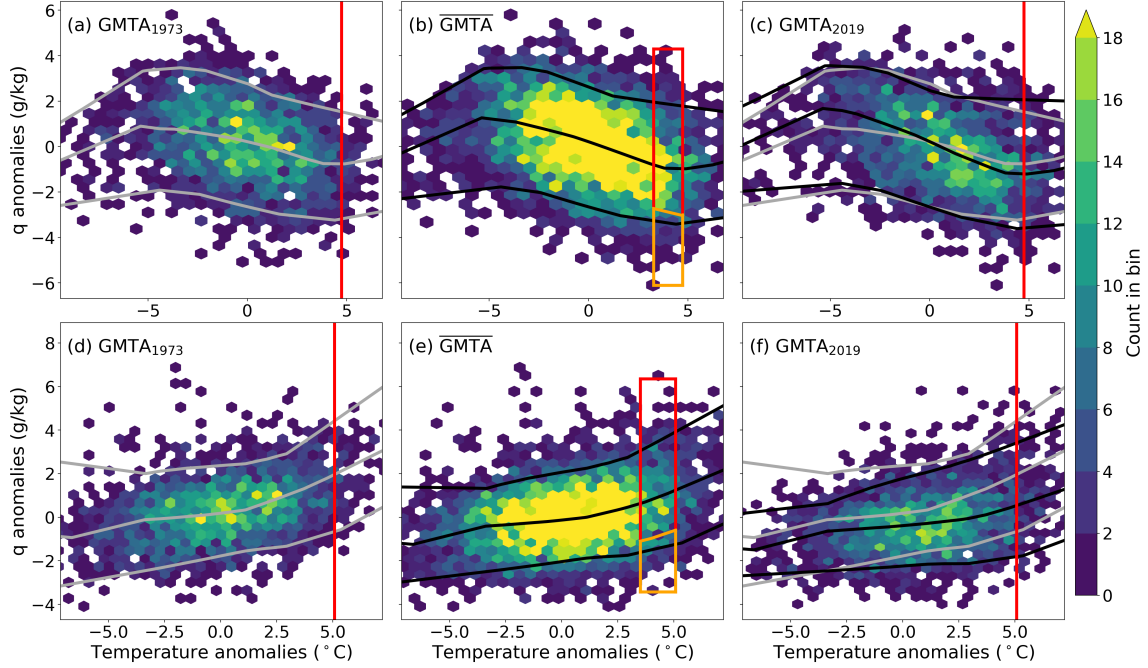


Figure 1: **Changes in the distribution of specific humidity as a function of increasing global mean temperature anomalies (GMTA) and local temperature.** Observed summer daily-average temperature and specific humidity from 1973-2019 at Perry Stokes Airport in southern Colorado (a-c) and Fresno Yosemite International Airport in central California (d-f) are shown as two-dimensional histograms. (a, d) Data from the first half of the record, and the quantile smoothing spline fit conditional on the 1973 lowpass filtered GMTA of -0.43°C . (b, e) Data from the full record, and the quantile smoothing spline fit conditional on the average GMTA (0°C by definition). (c, f) Data from the second half of the record, and the quantile smoothing spline fit conditional on the 2019 lowpass filtered GMTA of 0.51°C . The spline fits from panels (a, d) are reproduced in gray in panels (c, f) to show changes in the temperature-specific humidity relationship as a function of increasing GMTA. The vertical red line shows the 95th percentile of temperature anomalies calculated over the full record. The amplification index is defined graphically in (b, e) as the count of days in the orange polygon (hot and dry) normalized by those in the orange and red polygons (hot only).

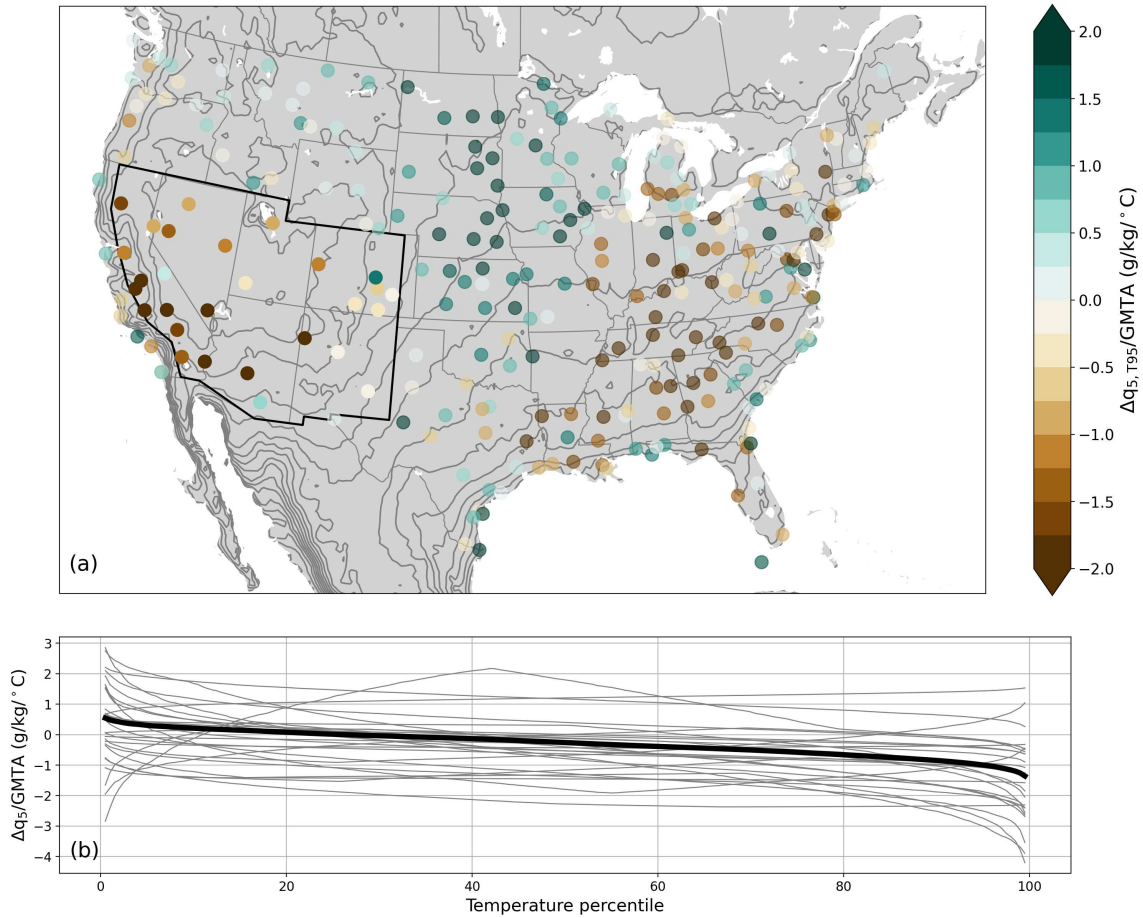


Figure 2: **Decreases in specific humidity in the American Southwest are amplified on hot days.** (a) Estimated changes in the 5th percentile of specific humidity on hot (95th percentile in temperature anomalies) days ($q'_{5,T95}$) for a 1°C increase in GMTA at high-quality ISD stations across the continental United States. The Southwest domain is outlined in black. Contours show the 5th percentile of July-August-September specific humidity from ERA5; the lowest contour is 3 g/kg , and the contour interval is 1 g/kg . (b) The estimated change in the 5th percentile of specific humidity (q'_5) as a function of temperature percentile at each station in the Southwest (thin grey lines) and the area-weighted average across stations (thick black line).

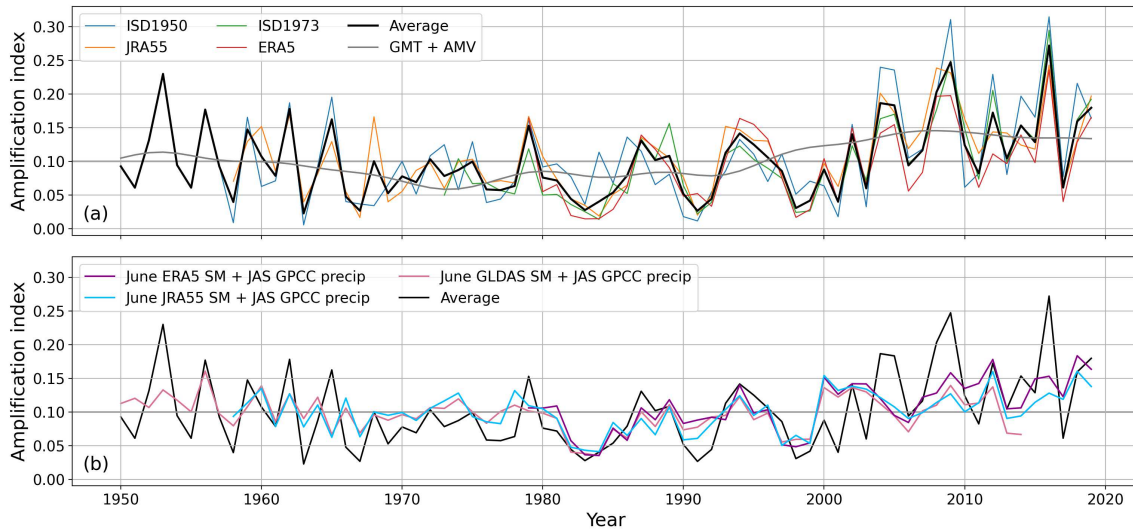


Figure 3: **The observed and fitted amplification index from 1950-2019.** (a) The amplification index estimated from four datasets (thin colored lines) and the average across the estimates (thick black line). Note that the number of datasets used to calculate the average changes over time as a function of dataset availability. The low-frequency behavior (gray line) is estimated based on a regression onto the GMTA and AMV, both which are lowpass filtered with a 1/10 year cutoff frequency. (b) The fitted amplification index using June soil moisture from three different datasets and summer precipitation. The average amplification index (black) is reproduced from (a).

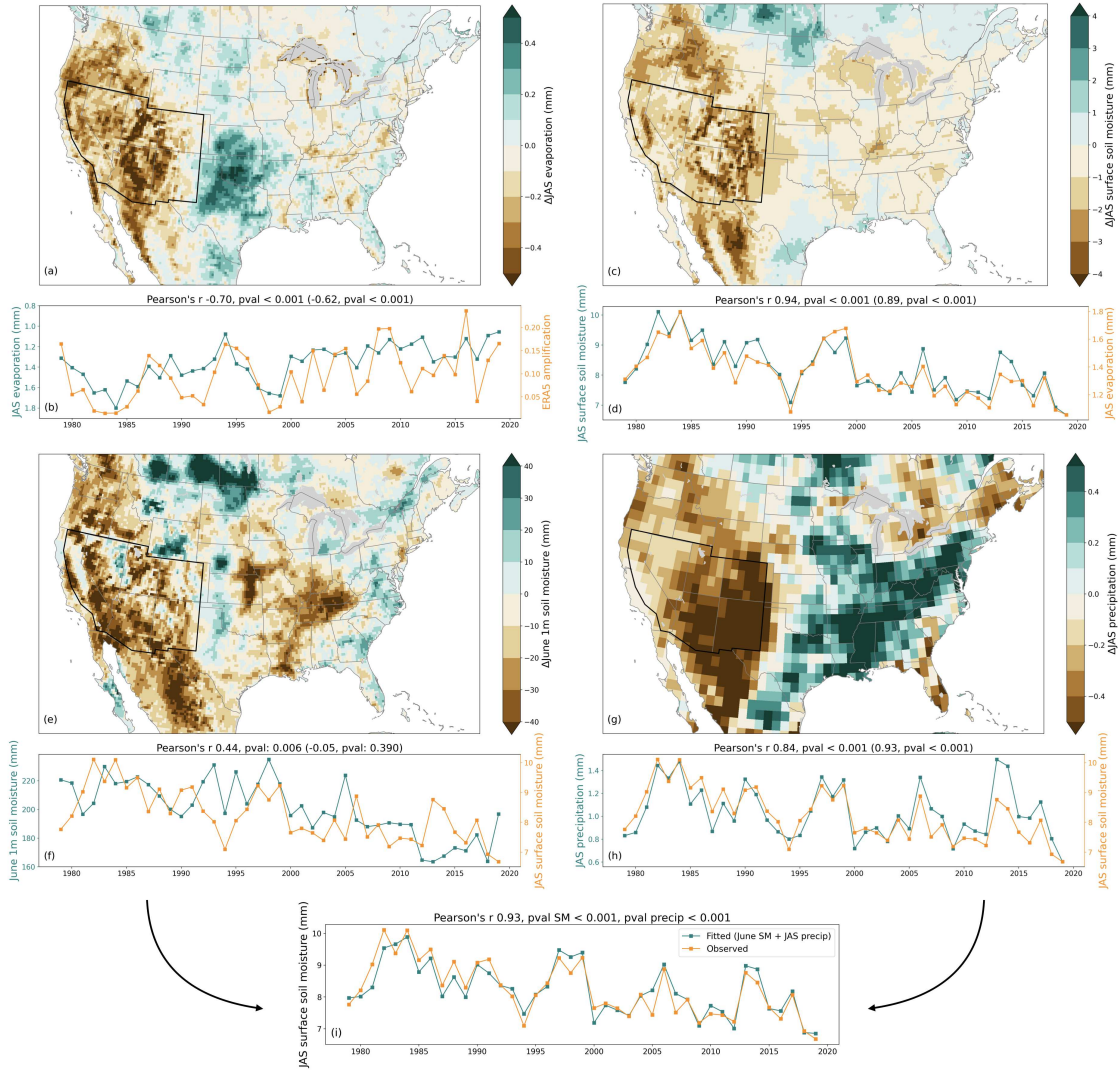


Figure 4: **Increased probability on hot, dry days linked to reduced surface evapotranspiration and soil moisture.** (a) The composite JAS evapotranspiration on years in the top tercile (33%) of the amplification index minus the bottom tercile. (b) The time series of the amplification index (orange) and the Southwest-average evapotranspiration (teal, y-axis inverted). (c) The composite JAS surface soil moisture on years in the bottom tercile of Southwest-average evapotranspiration minus the top tercile. (d) The time series of Southwest-average JAS evapotranspiration (orange) and JAS surface soil moisture (teal). (e) The composite June 1m soil moisture on years in the bottom tercile of Southwest-average JAS surface soil moisture minus the top tercile. (f) The time series of Southwest-average JAS surface soil moisture (orange) and June 1m soil moisture (teal). (g) The composite JAS precipitation on years in the bottom tercile of Southwest-average JAS surface soil moisture minus the top tercile. (h) The time series of Southwest-average JAS surface soil moisture (orange) and JAS precipitation (teal). (i) The observed (orange) and fitted (teal) JAS surface soil moisture; the fitted values are based on a multiple linear regression model using June 1m soil moisture and JAS precipitation as covariates. All data besides precipitation are from ERA5, whereas precipitation is from the Global Precipitation Climatology Centre. Evapotranspiration and precipitation are both the total per day. Raw (detrended) correlation and p-values for each time series are shown in the associated title.

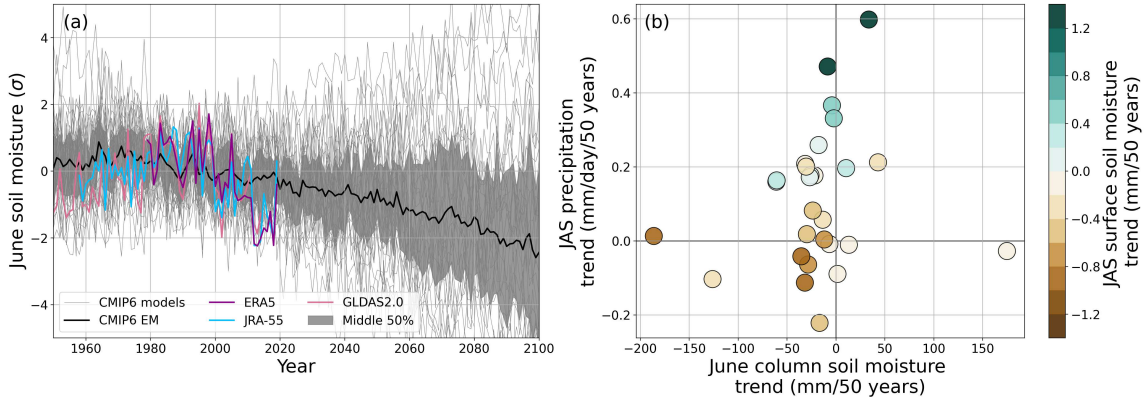


Figure 5: **CMIP6 projections of pre-summer column soil moisture, summer precipitation, and summer surface soil moisture.** (a) The June total column soil moisture in the CMIP6 models (gray lines, gray shading shows 50% range) and the ensemble mean (black line) from 1950-2100 using the historical and SSP5-8.5 scenarios. Three observational estimates of top 1m June soil moisture are shown in colors. All time series are normalized to have zero mean and unity variance for the overlapping period of 1979-2014. The CMIP6 models show a wide spread of behavior, although most models project decreases. (b) The relationship between the linear trend in June column soil moisture (horizontal axis), JAS precipitation (vertical axis), and JAS surface soil moisture (colors) across CMIP6 models. The CMIP6 models are split about trends in JAS surface soil moisture based on the extent to which precipitation increases counterbalance June soil moisture decreases. Trends are calculated over 2015-2100, and normalized to per 50 years.

Predictors: AMV and GMTA

Predictor name	Regression coefficient (95% range)	p-value
Lowpass GMTA	0.0597 (0.018, 0.101)	0.006
Lowpass AMV index	0.1253 (0.034, 0.217)	0.008
Nino3.4 index	-0.005 (-0.013, 0.012)	0.934
PDO index	0.0019 (-0.015, 0.019)	0.830

Predictors: Soil moisture and precipitation

Predictor name	Regression coefficient (95% range)	p-value
ERA5 soil moisture	-0.025 (-0.040, -0.010)	<0.001
GPCC precip (ERA5)	-0.026 (-0.041, -0.011)	<0.001
JRA-55 soil moisture	-0.017 (-0.029, -0.005)	0.004
GPCC precip (JRA-55)	-0.022 (-0.034, -0.010)	<0.001
GLDAS2.0 soil moisture	-0.013 (-0.024, -0.001)	0.014
GPCC precip (GLDAS2.0)	-0.023 (-0.034, -0.012)	<0.001

Table S1: Regression coefficients, 95% confidence intervals, and p-values associated with two multiple linear regression models for the amplification index. The AMV-GMTA fitted model is shown as the gray line in Fig. 3a. GMTA and the AMV index are lowpass filtered with a cutoff frequency of 1/10 years using a third-order Butterworth filter. The Nino3.4 index and PDO index are not used in the fitting of the AMV-GMTA model. The soil moisture and precipitation fitted model is shown as the colored lines in Fig. 3b. All fitted models use GPCC precipitation; the soil moisture product used in conjunction with the GPCC precipitation is shown in parentheses.

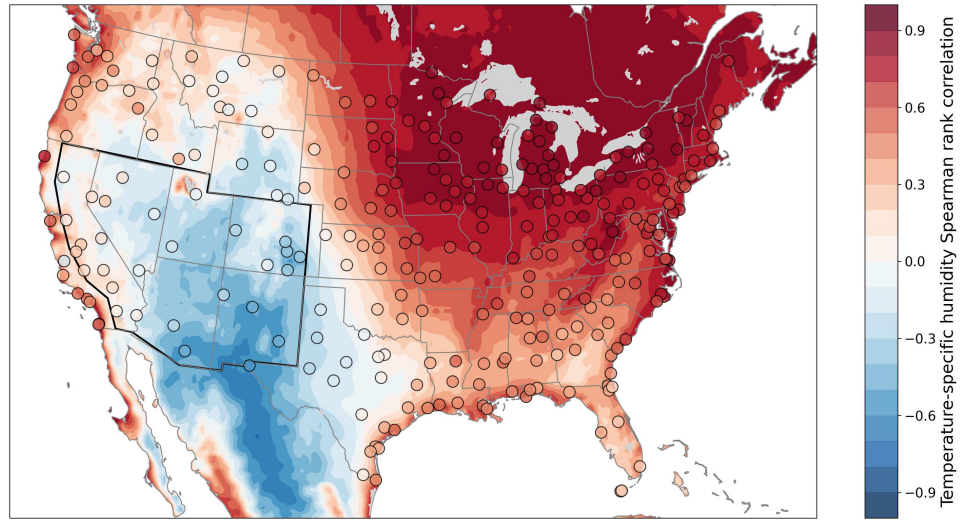


Figure S1: The Spearman rank correlation between July-August-September daily average temperature and specific humidity using ERA5 reanalysis (contours) and in situ station data from the Integrated Surface Database (circles).

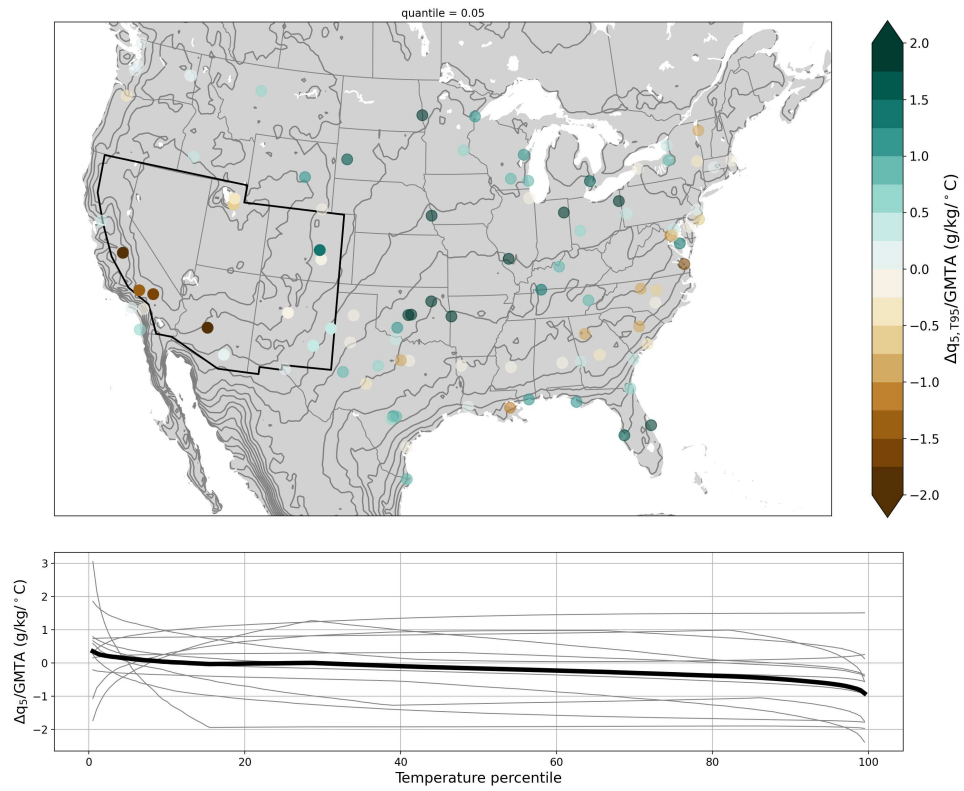


Figure S2: As in Fig. 2, but with the limited number of stations with data beginning in 1950.

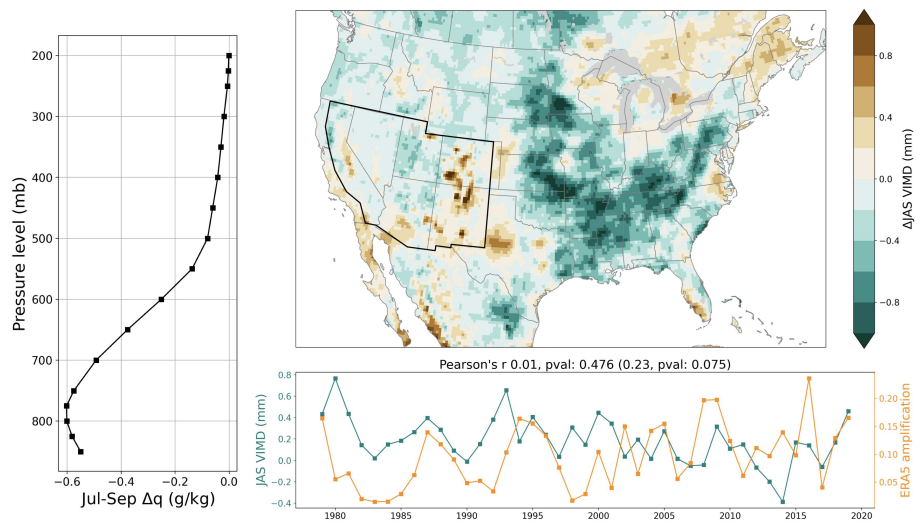


Figure S3: (Left) The vertical profile of specific humidity on top tercile minus bottom tercile amplification index years. (Right) As in Fig. 4, but for the vertically integrated moisture divergence from ERA5. Vertically integrated moisture divergence is total per day.

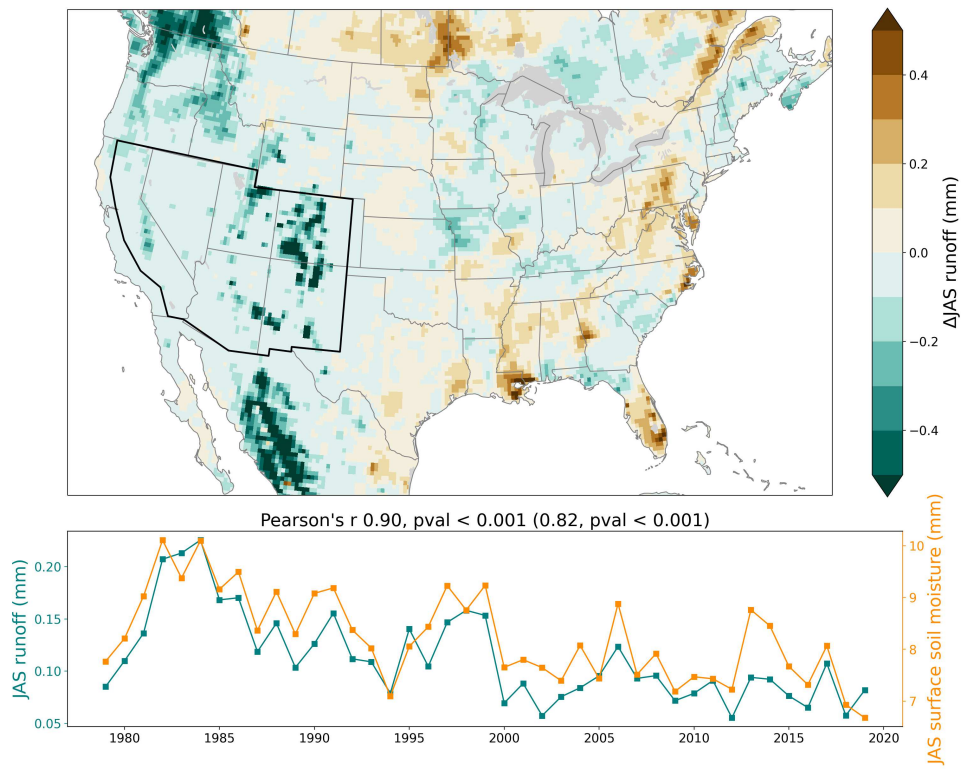


Figure S4: As in Fig. 4, but for runoff from ERA5. Runoff is the total per day.

Figures

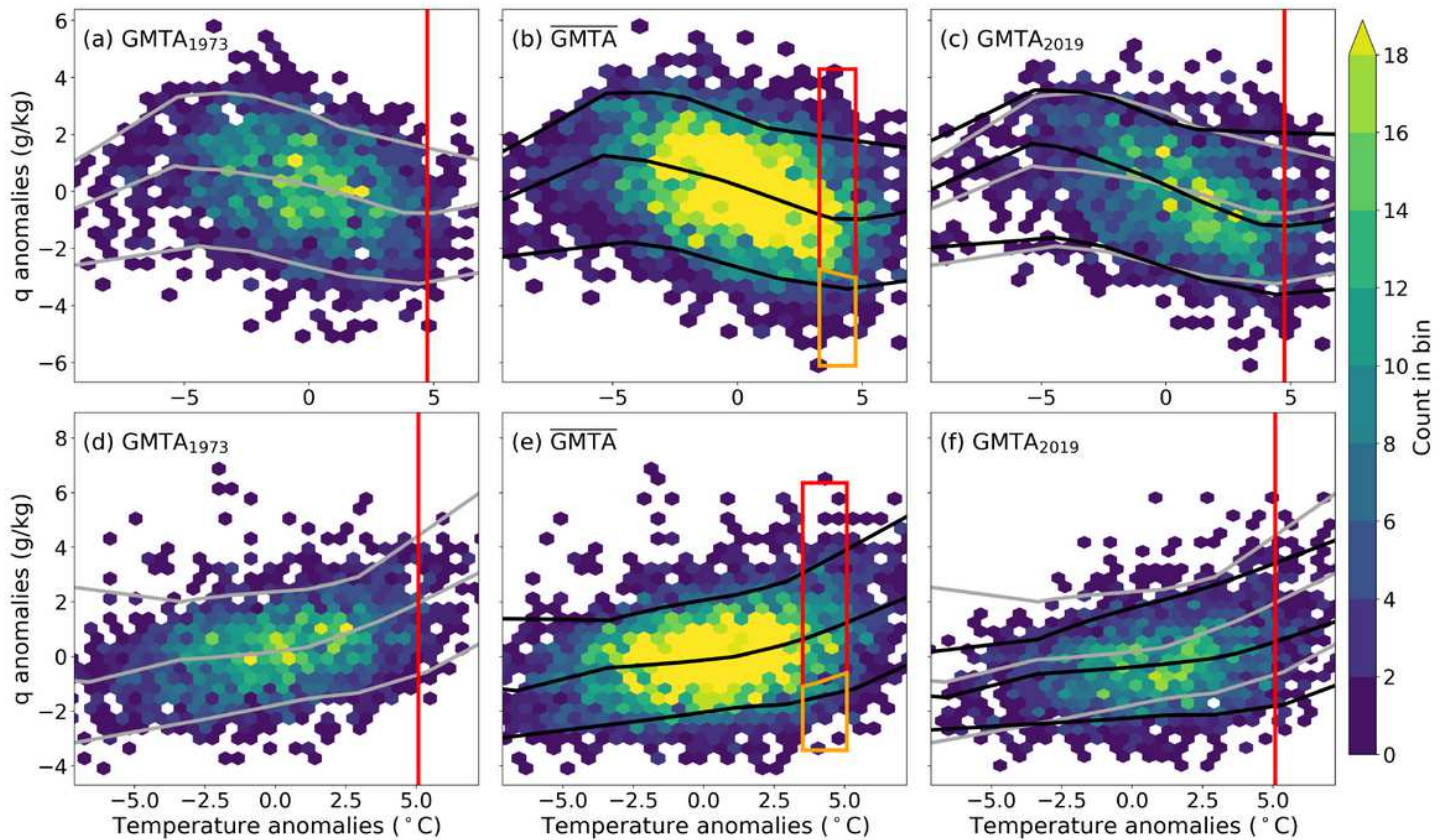


Figure 1

Changes in the distribution of specific humidity as a function of increasing global mean temperature anomalies (GMTA) and local temperature. Observed summer daily-average temperature and specific humidity from 1973-2019 at Perry Stokes Airport in southern Colorado (a-c) and Fresno Yosemite International Airport in central California (d-f) are shown as two-dimensional histograms. (a, d) Data from the first half of the record, and the quantile smoothing spline fit conditional on the 1973 lowpass filtered GMTA of -0.43°C . (b, e) Data from the full record, and the quantile smoothing spline fit conditional on the average GMTA (0°C by definition). (c, f) Data from the second half of the record, and the quantile smoothing spline fit conditional on the 2019 lowpass filtered GMTA of 0.51°C . The spline fits from panels (a, d) are reproduced in gray in panels (c, f) to show changes in the temperature-specific humidity relationship as a function of increasing GMTA. The vertical red line shows the 95th percentile of temperature anomalies calculated over the full record. The amplification index is defined graphically in (b, e) as the count of days in the orange polygon (hot and dry) normalized by those in the orange and red polygons (hot only).

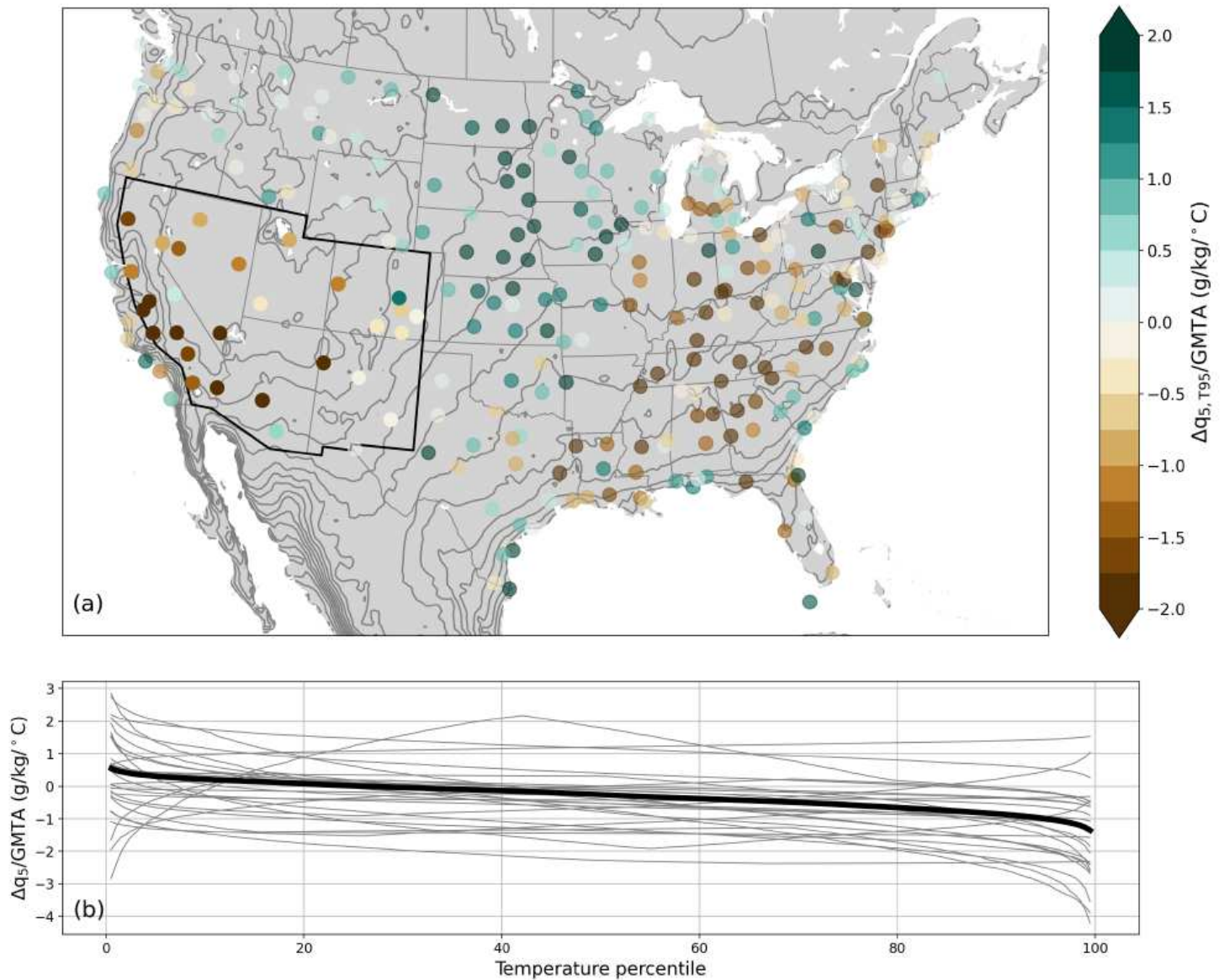


Figure 2

Decreases in specific humidity in the American Southwest are amplified on hot days. (a) Estimated changes in the 5th percentile of specific humidity on hot (95th percentile in temperature anomalies) days ($q_{05,T95}$) for a 1°C increase in GMTA at high-quality ISD stations across the continental United States. The Southwest domain is outlined in black. Contours show the 5th percentile of July-August-September specific humidity from ERA5; the lowest contour is 3 g/kg , and the contour interval is 1 g/kg . (b) The estimated change in the 5th percentile of specific humidity (q_{05}) as a function of temperature percentile at each station in the Southwest (thin grey lines) and the area weighted average across stations (thick black line).

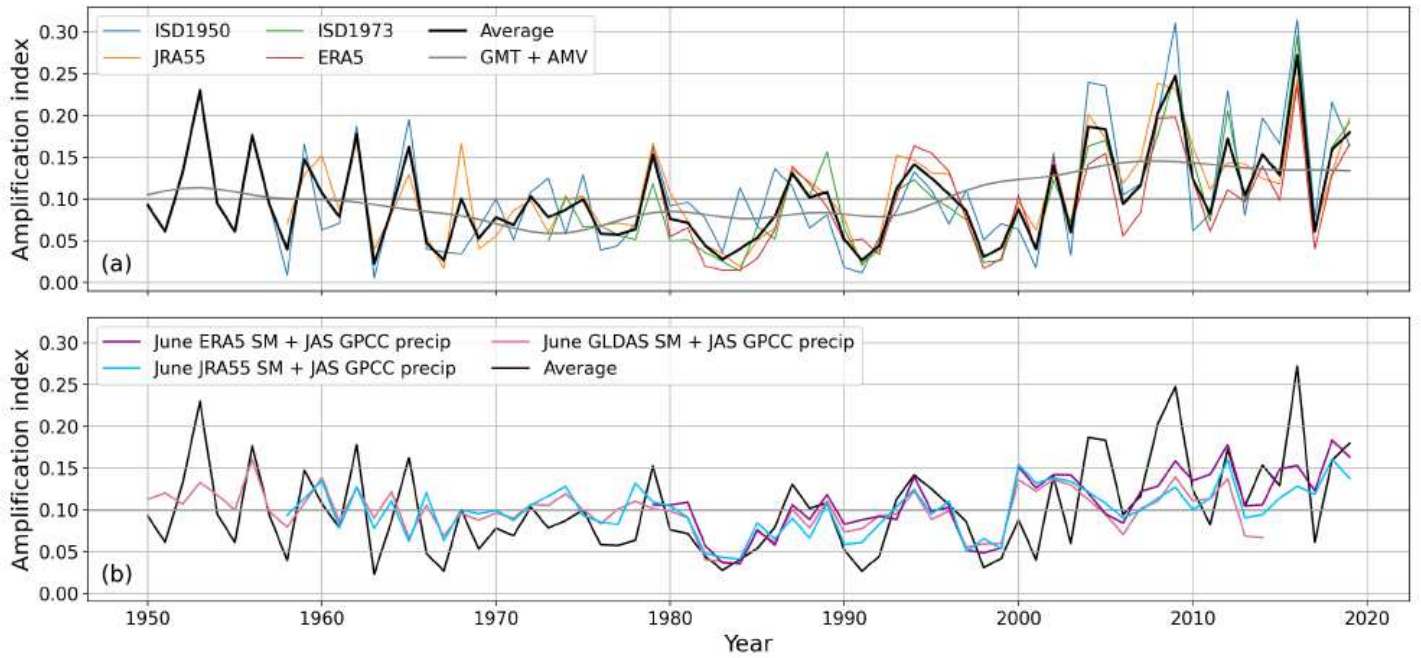


Figure 3

The observed and fitted amplification index from 1950-2019. (a) The amplification index estimated from four datasets (thin colored lines) and the average across the estimates (thick black line). Note that the number of datasets used to calculate the average changes over time as a function of dataset availability. The low-frequency behavior (gray line) is estimated based on a regression onto the GMTA and AMV, both which are lowpass filtered with a 1/10 year cutoff frequency. (b) The fitted amplification index using June soil moisture from three different datasets and summer precipitation. The average amplification index (black) is reproduced from (a).

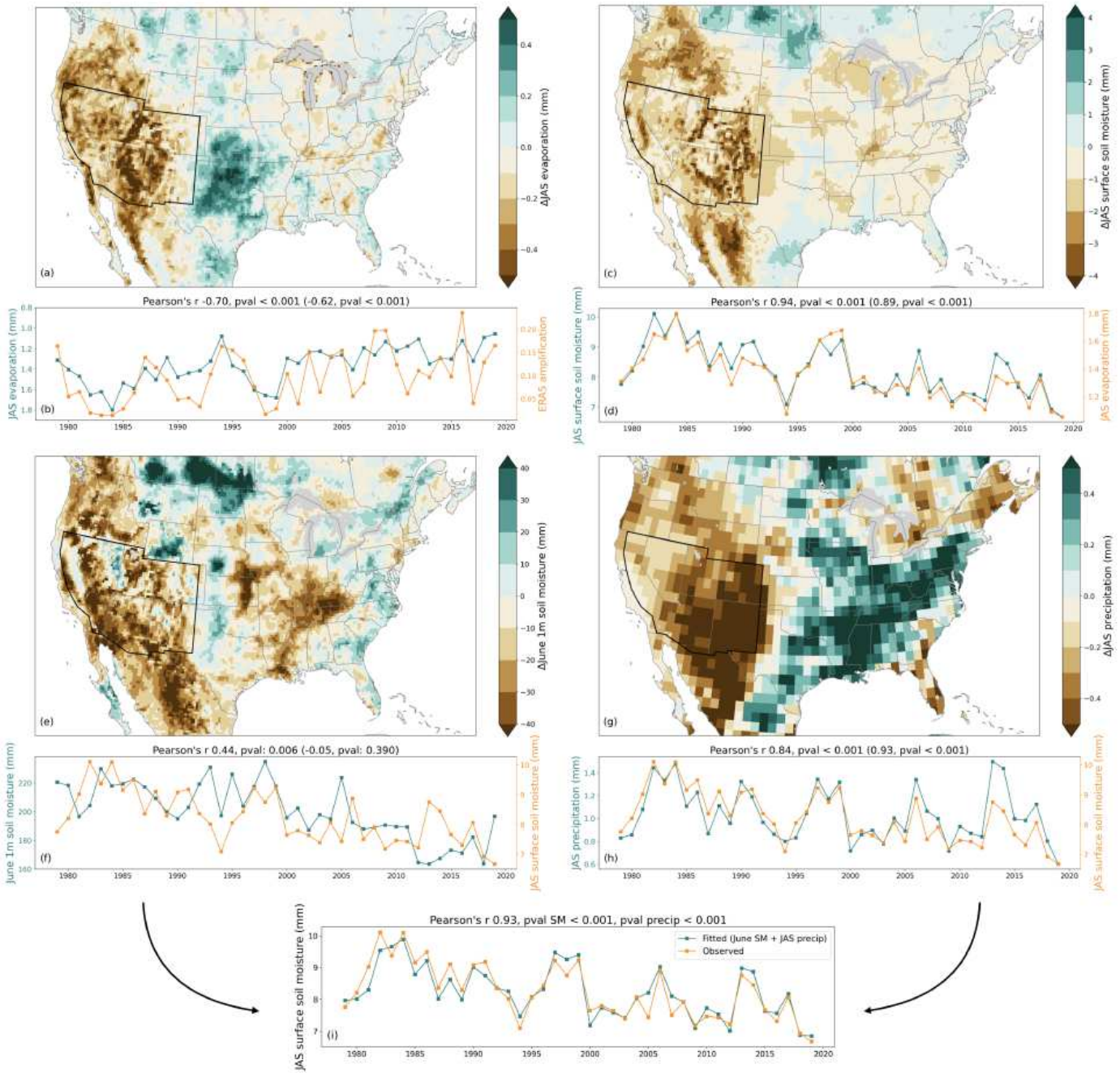


Figure 4

Increased probability on hot, dry days linked to reduced surface evapotranspiration and soil moisture. (a) The composite JAS evapotranspiration on years in the top tercile (33%) of the amplification index minus the bottom tercile. (b) The time series of the amplification index (orange) and the Southwest-average evapotranspiration (teal, y-axis inverted). (c) The composite JAS surface soil moisture on years in the bottom tercile of Southwest-average evapotranspiration minus the top tercile. (d) The time series of Southwest-average JAS evapotranspiration (orange) and JAS surface soil moisture (teal). (e) The composite June 1m soil moisture on years in the bottom tercile of Southwest-average JAS surface soil moisture minus the top tercile. (f) The time series of Southwest-average JAS surface soil moisture (orange) and June 1m soil moisture (teal). (g) The composite JAS precipitation on years in the bottom

tercile of Southwest-average JAS surface soil moisture minus the top tercile. (h) The time series of Southwest-average JAS surface soil moisture (orange) and JAS precipitation (teal). (i) The observed (orange) and fitted (teal) JAS surface soil moisture; the fitted values are based on a multiple linear regression model using June 1m soil moisture and JAS precipitation as covariates. All data besides precipitation are from ERA5, whereas precipitation is from the Global Precipitation Climatology Centre. Evapotranspiration and precipitation are both the total per day. Raw (detrended) correlation and p-values for each time series are shown in the associated title.

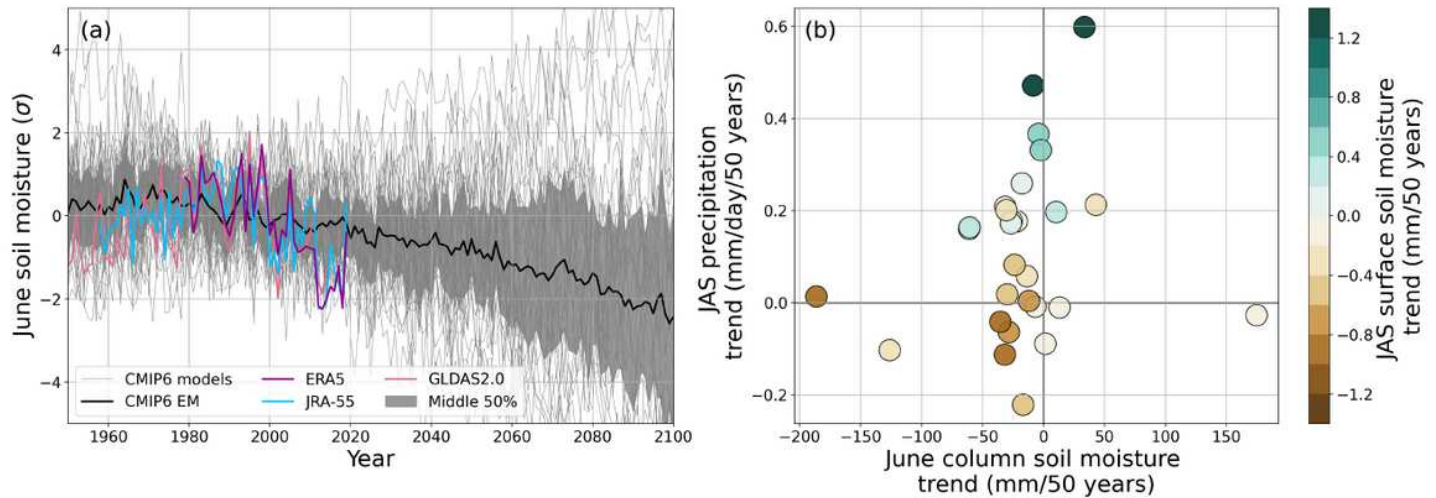


Figure 5

CMIP6 projections of pre-summer column soil moisture, summer precipitation, and summer surface soil moisture. (a) The June total column soil moisture in the CMIP6 models (gray lines, gray shading shows 50% range) and the ensemble mean (black line) from 1950-2100 using the historical and SSP5-8.5 scenarios. Three observational estimates of top 1m June soil moisture are shown in colors. All time series are normalized to have zero mean and unity variance for the overlapping period of 1979- 2014. The CMIP6 models show a wide spread of behavior, although most models project decreases. (b) The relationship between the linear trend in June column soil moisture (horizontal axis), JAS precipitation (vertical axis), and JAS surface soil moisture (colors) across CMIP6 models. The CMIP6 models are split about trends in JAS surface soil moisture based on the extent to which precipitation increases counterbalance June soil moisture decreases. Trends are calculated over 2015-2100, and normalized to per 50 years.